Check for updates

Investigation of Grain Growth in Chalcopyrite $CuInS_2$ Photoelectrodes Synthesized under Wet Chemical Conditions for Bias-Free Photoelectrochemical Water Splitting

Sang Youn Chae, Noyoung Yoon, Minki Jun, Sung Hyun Hur, Myeongjae Lee, BongSoo Kim, Jin Young Kim, Eun Duck Park, Jong Hyeok Park,* and Oh Shim Joo**

Photoelectrochemical (PEC) cells offer a promising method for producing green hydrogen through the splitting of water using solar energy. However, the cost-effective synthesis of highly crystalline p-type semiconductor materials for PEC cells remains a significant challenge for industrial applications. Herein, a $CuInS_2$ photoelectrode is fabricated using a scalable and economical wet chemical spin-coating technique. To enhance the crystallinity and photoelectrochemical activity of the photoelectrode, the grain size is precisely controlled by adjusting the atomic ratio, thickness, morphology, and Ag doping. Evaluating a novel growth mechanism of $CuInS_2$ from Cu–In–O reveals that Ag doping significantly promotes grain growth. Consequently, the $CuInS_2$ photocathode achieves one of the highest photoelectrochemical activities ($-9.8\ mA\ cm^{-2}$ at 0 V_{RHE}) reported for $CuInS_2$ photoelectrodes synthesized via wet chemical methods. Bias-free water splitting is achieved using a $CuInS_2$-based photoelectrode in a photovoltaic–PEC cell configuration. These results highlight the potential of $CuInS_2$, prepared through wet chemical methods, for cost-effective photoelectrochemical water splitting.

1. Introduction

Hydrogen is an attractive energy carrier owing to its high energy density ($142\ kJ\ g^{-1}$).[1] It can be produced by splitting water ($H_2O(l) \rightarrow H_2(g) + 1/2O_2(g)$, $\Delta H^0_{f,298\ K} = -285.8\ kJ\ mol^{-1}$) with an external energy supply, which is known to be an ideal solution to the intermittency of renewable energy.

Photoelectrochemical (PEC) cells offers a key approach for converting solar energy into chemical energy. These cells produce hydrogen through the splitting of water with photon energy. A PEC cell comprises a photoelectrode and a counter electrode, with the semiconductor photoelectrode primarily serving as the photoabsorber. The absorbed photons generate photoexcited charge carriers (electrons and holes) capable of driving the water redox reaction.

S. Y. Chae, E. D. Park
Department of Energy Systems Research
Ajou University
World Cup-ro 206, Suwon 16499, Republic of Korea
E-mail: edpark@ajou.ac.kr

S. Y. Chae
Ajou Energy Science Research Center
Ajou University
World Cup-ro 206, Suwon 16499, Republic of Korea

N. Yoon, O. S. Joo
Clean Energy Research Center
Korea Institute of Science and Technology
Hwarang-ro 14-gil 5, Seoul 02792, Republic of Korea
E-mail: joocat@kist.re.kr

N. Yoon, J. H. Park
Department of Chemical and Biomolecular Engineering
Yonsei University
Yonsei-ro 50, Seoul 03722, Republic of Korea
E-mail: lutts@yonsei.ac.kr

M. Jun, J. Y. Kim
Hydrogen·Fuel Cell Research Center
Korea Institute of Science and Technology
Hwarang-ro 14-gil 5, Seoul 02792, Republic of Korea

S. H. Hur, B. S. Kim
Graduate School of Semiconductor Materials and Device Engineering
Ulsan National Institute of Science and Technology (UNIST)
UNIST-gil 50, Ulsan 44919, Republic of Korea

M. Lee, B. S. Kim
Department of Chemistry
Ulsan National Institute of Science and Technology (UNIST)
UNIST-gil 50, Ulsan 44919, Republic of Korea

B. S. Kim
Graduate School of Carbon Neutrality
Ulsan National Institute of Science and Technology (UNIST)
Unist-gil 50, Ulsan 44919, Republic of Korea

E. D. Park
Department of Chemical Engineering
Ajou University
World Cup-ro 206, Suwon 16499, Republic of Korea

The ORCID identification number(s) for the author(s) of this article can be found under https://doi.org/10.1002/solr.202400518.

© 2024 The Author(s). Solar RRL published by Wiley-VCH GmbH. This is an open access article under the terms of the Creative Commons Attribution License, which permits use, distribution and reproduction in any medium, provided the original work is properly cited.

DOI: 10.1002/solr.202400518

In particular, H_2 can be photoelectrochemically generated via the hydrogen evolution reaction (HER) ($2H^+(aq) + 2e^- \rightarrow H_2(g)$) at the solid–liquid junction of a p-type semiconductor photoelectrode–electrolyte interface.[2]

Despite extensive research on n-type materials, such as TiO_2, $BiVO_4$, and WO_3, the progress in developing efficient p-type materials has not matched that of their counterparts. Consequently, the solar-to-hydrogen conversion efficiency (η_{STH}) of semiconductor photoelectrodes remains below theoretical expectations. PEC cells are projected to achieve 10–30% η_{STH} depending on the semiconductor bandgap and cell configuration;[3] however, the reported efficiencies for single or tandem PEC cells are only 1–3%. This can be attributed to rapid electron–hole recombination at the semiconductor electrodes and the high overpotential for the water decomposition reaction.[2,4–7]

To overcome the low η_{STH} of PEC cells, a photovoltaic (PV)–PEC cell is suggested.[8] In this configuration, a PV cell is connected in series to a PEC cell to supply additional voltage. Although various PV–PEC (tandem) cells have been reported, most focus on the combination of n-type materials (Fe_2O_3, $BiVO_4$, and Ta_3N_5) as photoanodes with PV cells (dye-sensitized, silicon, and perovskite solar cells)[9–15]. The external bias from the PV cells to the PEC cells allows for an advanced η_{STH} (2–7%) compared to a simple PEC cell; however, there are still much rooms for the improvement. One of the limiting factors of the PV–PEC cells is the poor onset potential and low photocurrent of the photoelectrode materials compared to the PV cells, due to carrier trapping at surface states or midgap sites in semiconductor materials.[16] Therefore, it is still necessary to develop the semiconductor materials with well-controlled properties, even when a PV–PEC configuration is applied.

Highly crystalline p-type semiconductor materials, such as p-Si, p-InP, and p-GaAs, exhibit high PEC efficiencies owing to the prolonged lifetime of charge carriers resulting from the low density of defects or trap sites. However, physical methods for preparing these materials, such as sputtering and coevaporation under ultrahigh-vacuum conditions, significantly increase the production costs of both the materials and hydrogen. Therefore, the development of cost-effective preparation methods for semiconductor thin films using wet chemical synthesis under nonvacuum conditions is crucial.

$CuInS_2$ exhibits a high absorption coefficient and a near-infrared-absorbable bandgap (≈1.5 eV), making it a promising candidate for photocathodes in PEC cells.[17,18] Moreover, $CuInS_2$ can be economically synthesized using various solution-based techniques, including electrodeposition, spin coating, spray pyrolysis, solvothermal approaches, wet chemical synthesis, and successive ionic layer adsorption and reaction.[19–30] However, the observed PEC H_2 production efficiency of $CuInS_2$ photoelectrodes, as indicated by their photocurrent density (0.02–16 mA cm^{-2}), deviates notably from the theoretical performance (≈28.96 mA cm^{-2}) predicted from the bandgap of $CuInS_2$.[18] This reduced activity can be primarily attributed to the rapid recombination of charge carriers resulting from the suboptimal crystallinity of $CuInS_2$ synthesized via solution-based methods. Thus, developing a method for synthesizing $CuInS_2$ with large, highly crystalline grains is imperative.

In this study, a spin-coating method was used to prepare $CuInS_2$ thin films as model p-type semiconductor materials for highly active and cost-effective photoelectrodes. The preparation involved coating the precursor ink containing Cu^{2+} and In^{3+} dissolved solutions onto the substrates, followed by thermal annealing. The spin-coating method offers several advantages for the preparation of thin-film semiconductors. This allows the precise control of the atomic ratio of semiconductors or doped heteroatoms by adjusting the composition of the precursor ink. Additionally, this approach facilitates mass production using roll-to-roll processes, making it cost-effective for film synthesis. Moreover, compared to other methods, such as electrodeposition or solvothermal synthesis, the spin-coating method is particularly effective for doping heteroatoms. This is because it facilitates the use of a dopant-mixed precursor ink.

To enhance the physical properties and PEC activity of the $CuInS_2$ films, various spin-coating parameters, including atomic ratio, doping, and sulfurization temperature, were optimized. Moreover, the formation mechanism of $CuInS_2$ thin film from the Cu–In–O films was investigated in detail to increase the grain size and PEC activity of the $CuInS_2$ thin films. As a result of fast recrystallization of $CuInS_2$ with Ag cation, an Ag-doped $CuInS_2$ (Ag:$CuInS_2$) film was successfully synthesized using the spin-coating method with an Ag-containing precursor ink. This film exhibited the highest PEC H_2 production activity (−9.8 mA cm^{-2} at 0 V vs reversible hydrogen electrode (RHE)) compared to previously reported $CuInS_2$ photocathodes prepared by wet chemical methods.[19–29] Furthermore, a PV cell (PV)–PEC cell with an optimized $CuInS_2$ photocathode demonstrated bias-free water splitting with a solar-to-hydrogen conversion efficiency of 4.15%. This is the first demonstration of a PV–PEC cell using a $CuInS_2$ photocathode.

2. Results and Discussion

2.1. Effect of Cu/In Ratios in $CuInS_2$ Thin Films for PEC H_2 Evolution

First, the effect of the Cu atomic ratio on $CuInS_2$ was investigated. It has been reported that the A/B atomic ratio in the chalcopyrite structure (ABX_2) can affect its PEC activity.[31,32] Therefore, the atomic ratio of Cu/In was controlled by adjusting the concentration of $Cu(NO_3)_3{\cdot}xH_2O$ in the precursor ink. Subsequently, the PEC activity of $CuInS_2$, which was controlled by the Cu/In ratio, was measured by linear sweep voltammetry (LSV) in an acidic electrolyte (0.1 M $HClO_4$) (**Figure 1**a). It is worth noting that chalcopyrite-based photocathodes are commonly tested in neutral or mildly basic electrolytes. However, acidic electrolytes can also be effective for overall water splitting, as they promote both HER with a Pt cocatalyst-decorated photocathode and OER with a noble metal oxide-based catalyst at the anode. Additionally, strong acidic electrolytes exhibit low solution resistance, which reduces energy loss in electrochemical devices.

In LSV measurements, all the samples exhibited similar onset potentials but different photocurrent values depending on the Cu/In ratio. Notably, the highest photocurrent was observed for $CuInS_2$ with a Cu/In ratio of 1:1 in the precursor ink. Rather, the excessive Cu/In ratio had a negative effect on the photocurrent of $CuInS_2$ (Figure 1b).

© 2024 The Author(s). Solar RRL published by Wiley-VCH GmbH

2367198x, 2024, 20, Downloaded from https://onlinelibrary.wiley.com/doi/10.1002/solr.202400518 by Cochrane Peru, Wiley Online Library on [01/10/2026]. See the Terms and Conditions (https://onlinelibrary.wiley.com/terms-and-conditions) on Wiley Online Library for rules of use; OA articles are governed by the applicable Creative Commons License

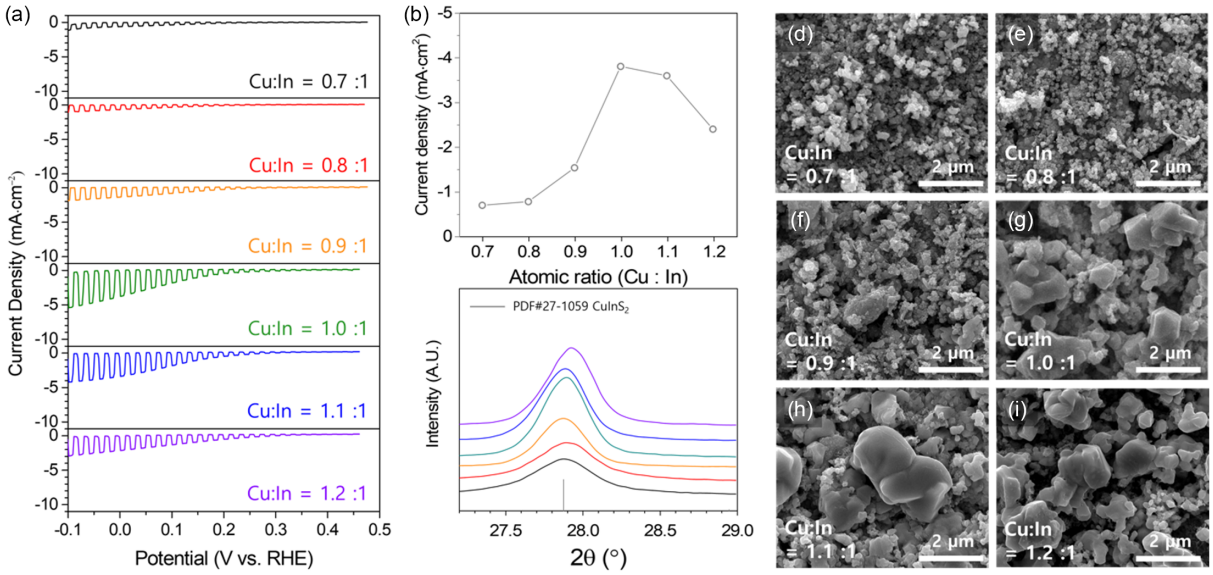

Figure 1. a) LSV results of $CuInS_2$ photocathodes, varying with the Cu/In ratio in the precursor ink. b) Comparison of the photocurrent density of the $CuInS_2$ at 0 V versus RHE. c) XRD patterns of the $CuInS_2$, varying with the Cu/In ratio in the precursor ink. d–i) SEM images of $CuInS_2$ with different Cu/In ratios in the precursor ink. All samples were prepared by repeating the spin-coating/calcination step three times.

The crystal phase and crystallinity of $CuInS_2$, which were controlled by the atomic ratio, were investigated through X-ray diffraction (XRD) (Figure 1c and S1, Supporting Information). The chalcopyrite $CuInS_2$ crystal phase was confirmed for all samples, but different full width half maximum (FWHM) at the (112) peak can be confirmed by the different atomic ratio of Cu:In. The grain size and photocurrent increased significantly when the Cu:In atomic ratio was 1:1. In particular, increasing the atomic ratio resulted in a narrower FWHM, indicating a larger grain size. Therefore, a larger grain size could lead to a higher photocurrent density owing to a lower chance of recombination at the grain boundary.[33,34] In addition, an XRD peak shift was observed for the Cu:In atomic ratio of 1.2:1. This could be due to lattice distortion caused by excessive Cu in the $CuInS_2$ lattice.

The absorption and optical bandgap of $CuInS_2$ with different Cu/In ratios were investigated using Kubelka–Munk absorption and Tauc plots (Figure S2, Supporting Information). A similar optical bandgap (1.48–1.5 eV) was estimated for all samples with different Cu/In atomic ratios, suggesting that bandgap size or light absorption is not the significant factor contributing to the differences in PEC activity. Mott–Schottky analysis was also performed on $CuInS_2$ (Figure S3, Supporting Information), revealing the carrier concentration and flat-band potential of the semiconductor material. Despite varying Cu/In ratios, there was no significant difference in the flat-band potential (≈1.1 V_{RHE}), which is related to the band position of the semiconductor material. However, the slope of the Mott–Schottky plot, which is inversely proportional to carrier concentration, increased significantly with increasing Cu/In ratios. Occasionally, Cu vacancies in chalcopyrite materials generate additional acceptors, resulting in stoichiometric $CuInS_2$ having a lower concentration of charge carriers. Nevertheless, high carrier concentration is not the only decisive factor for high PEC activity of semiconductor materials.

The morphology of the thin film and its grain size are also important factors influencing the PEC activity of the semiconductor. Therefore, further investigation of the grain size of $CuInS_2$ was conducted using scanning electron microscopy (SEM) (Figure 1d–i). Tens of nanometer-sized $CuInS_2$ grains were found in the $CuInS_2$ prepared from the precursor inks, when the atomic ratio of Cu/In is less than 1. On the other hand, hundreds of nanometer-sized $CuInS_2$ crystal grains were observed in the $CuInS_2$ film prepared with Cu:In atomic ratios ranging from 1:1 to 1.2:1. These results agree with the FWHM of the XRD peak; that is, the high Cu content in the precursor ink provided $CuInS_2$ with a larger grain size. The atomic ratio of the precursor ink is critical for the final grain size of $CuInS_2$ and affects the photocurrent density of the $CuInS_2$ film. The $CuInS_2$ film prepared with a Cu:In ratio of 1:1 exhibited large grains and the highest photocurrent among the atomic-ratio-controlled $CuInS_2$. Therefore, the Cu:In atomic ratio of the precursor ink was fixed at 1:1 for the subsequent experiments.

2.2. Effect of Spin-Coating Cycles for the Thickness and Morphology of $CuInS_2$ Thin Films

The thickness of the photoelectrode film is a crucial factor for increasing the photocurrent density of the semiconductor photoelectrode, as it is directly related to the light absorption and diffusion length of the charge carriers. Therefore, the spin-coating/calcination steps were repeated 1, 3, 6, 9, and 12 times to control the film thickness. The photocurrent of $CuInS_2$ was investigated through LSV measurements and compared for different numbers of coating cycles (**Figure 2**a,b). The photocurrent value increased proportionally with the number of coating cycles up to the 9th cycle but decreased at the 12th coating cycle. The film thicknesses and surface morphologies of $CuInS_2$ with different

© 2024 The Author(s). Solar RRL published by Wiley-VCH GmbH

2367198x, 2024, 20, Downloaded from https://onlinelibrary.wiley.com/doi/10.1002/solr.202400518 by Cochrane Peru, Wiley Online Library on [01/10/2026]. See the Terms and Conditions (https://onlinelibrary.wiley.com/terms-and-conditions) on Wiley Online Library for rules of use; OA articles are governed by the applicable Creative Commons License

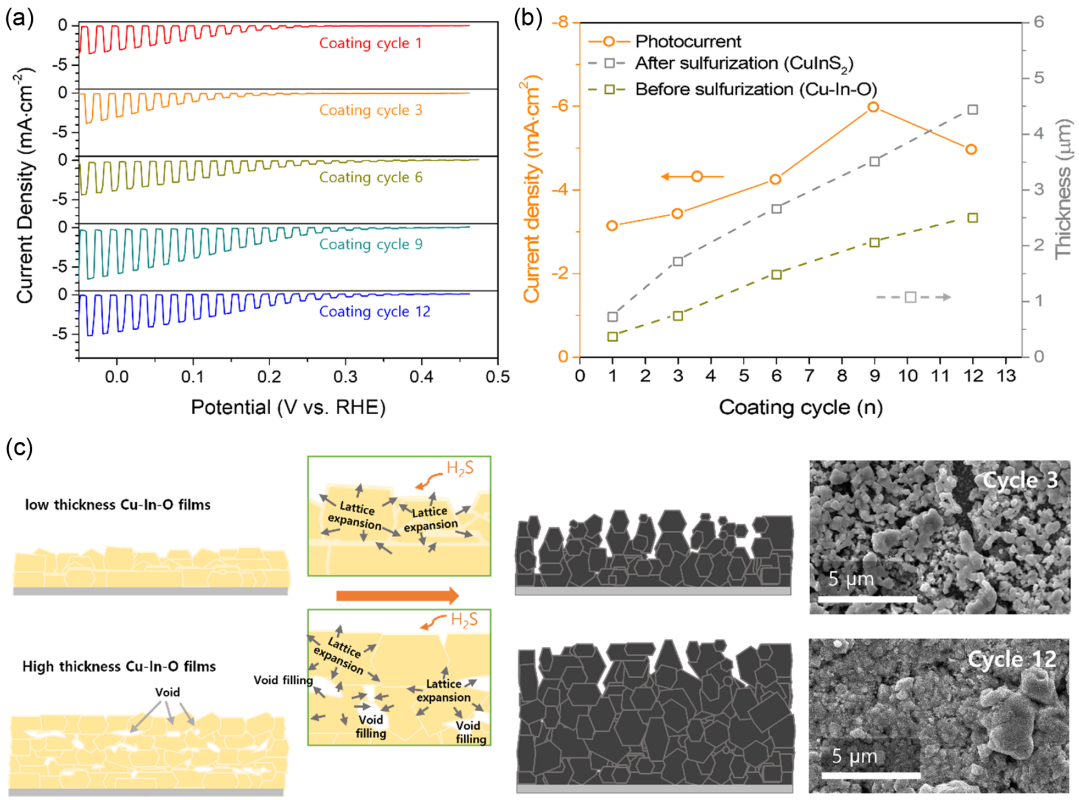

Figure 2. a) LSV results of $CuInS_2$ photocathodes, varying with the number of spin-coating–calcination cycles. b) Comparison of the photocurrent and film thickness of the $CuInS_2$ and calcined films (Cu–In–O), depending on the number of spin-coating–calcination cycles. c) Schematic diagram of the morphology changes in the Cu–In–O after sulfurization. SEM images of the $CuInS_2$ with different numbers of spin-coating–calcination cycles (3 and 12).

numbers of coating cycles were investigated using cross-sectional and top-view SEM images (Figure S4, Supporting Information). With the increase in the coating cycles, the thickness of $CuInS_2$ proportionally increased from 0.72 (1st cycle) to 4.44 μm (12th cycle). Therefore, higher light absorption can be achieved with repeated coating owing to the increased film thickness.

In addition, changing the surface morphology of $CuInS_2$ by increasing the number of coating cycles affected the photocurrent. With an increasing number of coating cycles, the surface cracks and porosity decreased owing to the aggregation of the $CuInS_2$ nanocrystalline particles. Charge carrier transportation can be improved with enhanced grain distribution, and to improve charge transfer, an enlarged grain size along with a well-stacked grain structure is important.[35] Notably, the thickness of the as-calcinated film after spin coating (Cu–In–O) increased approximately twofold after sulfurization. This result indicates that the surface crack formation on $CuInS_2$ was induced by the lattice expansion of the densely deposited Cu–In–O films during the sulfurization steps (Figure 2c). However, more voids were observed in the inner part of the Cu–In–O films when the number of coating cycles was increased (refer to the cross-sectional SEM images in Figure S4, Supporting Information). In this case, lattice expansion during sulfurization was conducted by filling the voids in the Cu–In–O films, resulting in a less porous $CuInS_2$ film (Figure 2c). However, for the 12th cycle, the photocurrent decreased despite the highest thickness and least porous surface morphology. This could be attributed to the increased bulk recombination of charge carriers derived from the longer path for charge transport to the semiconductor–electrolyte interface.[36] Indeed, the light absorption of $CuInS_2$ increases with the number of coating cycles, but it saturates after nine cycles (Figure S5, Supporting Information). Therefore, the ninth cycle was selected to obtain the optimal thickness.

Based on the atomic ratio and thickness control results, we conclude that the well-packed and large-grain structure of $CuInS_2$ is strongly related to its high photocurrent density. Therefore, the sulfurization of the Cu–In–O films was further investigated. Generally, $CuInS_2$ is formed by recrystallization from Cu_2S and In sources.[37] Various synthesis methods initiate the recrystallization process via Cu_2S formation with H_2S from Cu–In alloy metals.[37–39] Because Cu–In metals have high reactivity with H_2S, $CuInS_2$ films with microsized grains can be obtained. However, in this study, partial oxide phases (Cu–In–O) were obtained via calcination before sulfurization to decompose the precursor and additives in the precursor ink. Therefore, the lower reactivity of Cu–In–O with H_2S than that of Cu–In may be the reason for its smaller grain size compared with that of the metallic Cu–In system. Sulfurization involves two steps: 1) preannealing the Cu–In–O films under a N_2 atmosphere and 2) reaction with H_2S gas. To identify the crystal phase changes during

© 2024 The Author(s). Solar RRL published by Wiley-VCH GmbH

2367198x, 2024, 20, Downloaded from https://onlinelibrary.wiley.com/doi/10.1002/solr.202400518 by Cochrane Peru, Wiley Online Library on [01/10/2026]. See the Terms and Conditions (https://onlinelibrary.wiley.com/terms-and-conditions) on Wiley Online Library for rules of use; OA articles are governed by the applicable Creative Commons License

the sulfurization process, XRD analysis was performed for the Cu–In–O film (calcined and preannealed films) and the final sulfurization film ($CuInS_2$) (**Figure 3**a). The initially calcined film consists of a mixture of CuO and In_2O_3. However, the broad peaks of In_2O_3 and CuO indicate the poor crystallinity of the oxide film owing to the mild calcination temperature (300 °C). Moreover, the phase transition was observed when the film was annealed under the N_2 atmosphere at 520 °C. The peak of In_2O_3 became intense and sharp; however, the peak of CuO diminished and a new peak of Cu_2O appeared. The morphologies of the calcined and preannealed films were confirmed through SEM (Figure S6, Supporting Information), and the completely changed particle shape of Cu–In–O was in agreement with the phase transition observed in the XRD results. Finally, after sulfurization, only the peak of $CuInS_2$ was observed, as shown in Figure 3a. Based on the XRD patterns, it is assumed that the preannealing step is beneficial for sulfurization because Cu_2O can easily react with H_2S to form Cu_2S. However, it remains unclear whether In_2O_3 is sufficiently reactive for rapid recrystallization from Cu_2S. Therefore, the sulfurization temperature was also controlled at 200–520 °C, and XRD patterns were obtained for each resulting film (Figure 3b). Interestingly, the $CuInS_2$ phase was successfully formed even at a very low temperature of 200 °C. These results suggest that the preannealed Cu–In–O film has sufficient reactivity with H_2S for recrystallization. The only difference that depended on the sulfurization temperature was the grain size of $CuInS_2$. Sharpening of the XRD peaks of $CuInS_2$ was observed with increasing sulfurization temperature. The SEM images also revealed that larger grains were formed at higher sulfurization temperatures (Figure S7, Supporting Information).

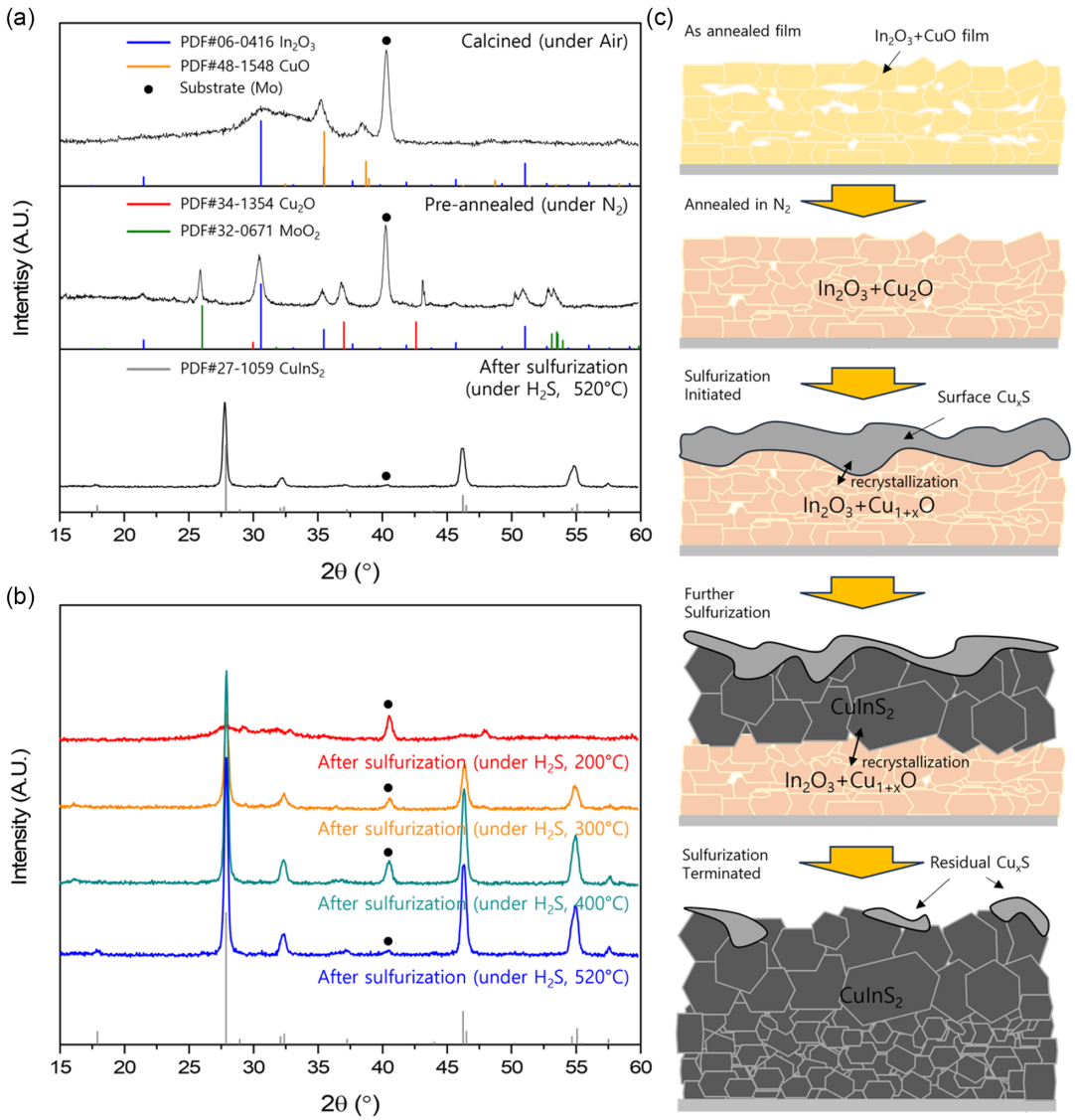

Figure 3. a) XRD patterns of a spin-coated–calcined film ($CuO + In_2O_3$), a preanneal film ($Cu_2O + In_2O_3$), and a sulfurized film ($CuInS_2$). b) XRD patterns of $CuInS_2$ films with different sulfurization temperature. c) Schematic diagram for sulfurization process of Cu–In–O films.

© 2024 The Author(s). Solar RRL published by Wiley-VCH GmbH

2367198x, 2024, 20, Downloaded from https://onlinelibrary.wiley.com/doi/10.1002/solr.202400518 by Cochrane Peru, Wiley Online Library on [01/10/2026]. See the Terms and Conditions (https://onlinelibrary.wiley.com/terms-and-conditions) on Wiley Online Library for rules of use; OA articles are governed by the applicable Creative Commons License

Regardless of the sulfurization temperature, the absorption edge (≈860 nm) was nearly the same, while higher scattering is observed in the longer wavelength region for the samples sulfurized at lower temperatures, as seen from the Kubelka–Munk absorption spectra (Figure S8, Supporting Information). This is consistent with the XRD results: $CuInS_2$ crystal is formed regardless of sulfurization temperatures, but the small grain size of $CuInS_2$ leads to the increased light scattering. It was confirmed that the slope of the Mott–Schottky plot increases with higher annealing temperatures, while the flat band potential remains almost constant (1.05–1.1 V_{RHE}) (Figure S9, Supporting Information). The value of slope is inversely proportional to the concentration of charge carriers. Therefore, as the sulfurization temperature increases, the crystallinity of $CuInS_2$ improves, which leads to the decrease in the concentration of atomic vacancies which generate charge carriers or serve as trap sites. As a result, annealing at higher temperatures leads to higher photocurrent and more positive onset potential for the $CuInS_2$ photocathode (Figure S10, Supporting Information). These support that the differences in grain size are critical for the PEC activity. Larger grains result in fewer grain boundaries, which can act as charge recombination sites, as previously discussed.

According to the recrystallization process model, cation exchange (particularly Cu^+) is a critical factor for fast and large grain growth.[40–42] $CuInS_2$ was prepared from Cu_2S via a topotactic reaction. In^{2+} replaced the vacancies of Cu^+ in Cu_2S, and sphalerite- or CuPt-phase $CuInS_2$ was prepared owing to the similarity in the crystal arrangement between Cu_2S and $CuInS_2$. During this process, In atoms diffused to the surface of the Cu_2S grains and occupied one-quarter of the tetrahedral sites initially occupied by Cu. Finally, the metastable sphalerite or CuPt-type $CuInS_2$ is transformed into a stable chalcopyrite phase.[43,44] This indicates that a high sulfurization temperature is more effective for improving cation mobility rather than overcoming the activation energy of the $CuInS_2$ formation reaction. Figure 3c summarizes the formation mechanism of $CuInS_2$ from the spin-coated Cu–In–O film through sulfurization, which is similar to that of the Cu–In metal system. This scheme also explains the grain-size differences between the surface and bottom (Figure S4, Supporting Information). Because Cu_2S, which was formed at the surface after preannealing, initiated the recrystallization process, the grain growth of $CuInS_2$ at the surface was more active than that on the subsurface.

2.3. Enhanced Grain Growth with Ag Doping

To increase the grain size of $CuInS_2$, the addition of Ag dopants can be effective for spin coating. During sulfurization, Ag cations were formed as $(Cu, Ag)_2S$ with H_2S and participated in the recrystallization of $CuInS_2$.[40] The higher mobility of Ag cations compared to that of Cu cations in $(Cu, Ag)InS_2$ increases the grain growth of chalcopyrite crystal.[45] The addition of Ag lowers the onset temperature of grain growth; therefore, the presence of Ag lowers the activation energy of the recrystallization process.[40] $CuInS_2$ films were prepared using Ag precursor-containing ink (1–10 at% vs Cu). The presence of Ag atoms in $CuInS_2$ was confirmed through X-ray photoelectron spectroscopy (XPS) (**Figure 4**a). The binding energy of the Ag $3d_{5/2}$ peaks (367.88 eV) indicated that the chemical state of Ag was not Ag_2S or Ag^0 (368.1 or 368.3 eV), but rather the oxidation state of Ag was +1 without any other states. The XRD pattern of

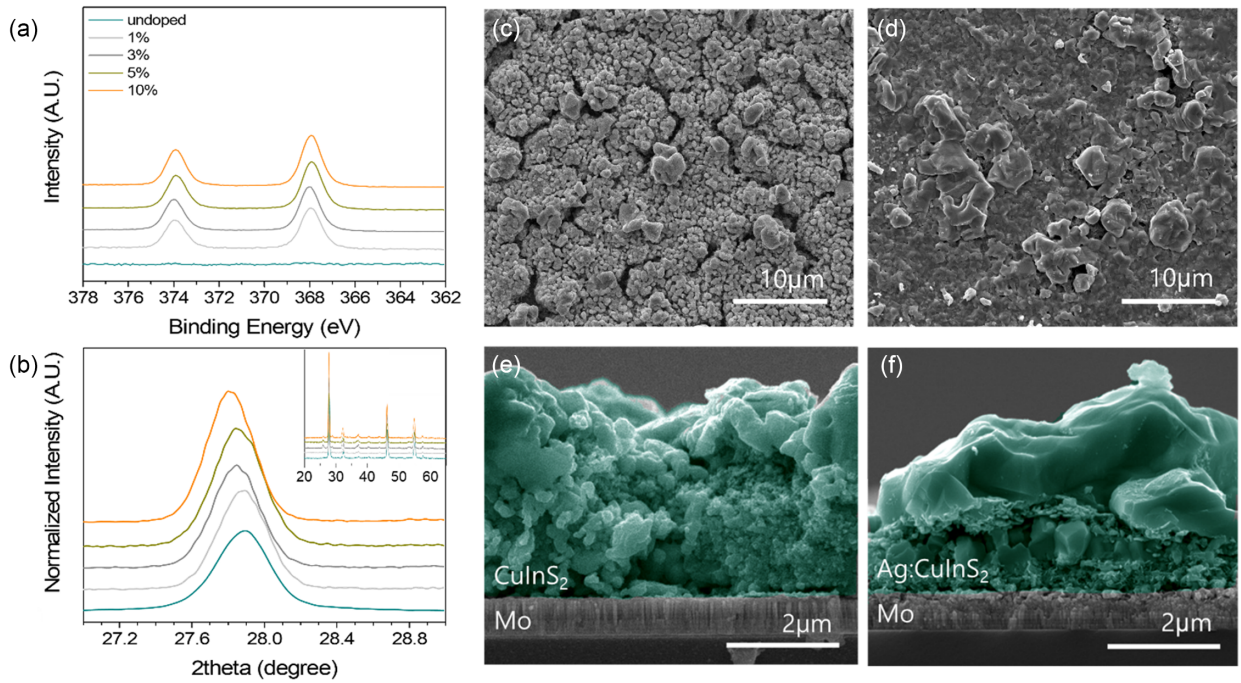

Figure 4. a) XPS spectra of Ag 3*d* from both undoped and Ag-doped $CuInS_2$ surface. b) XRD results of undoped and Ag-doped $CuInS_2$ thin films. c) SEM image of $CuInS_2$ (top view). d) SEM image of 3% Ag-doped $CuInS_2$ (top view). e) SEM image of $CuInS_2$ (cross-sectional view). f) SEM image of 3% Ag-doped $CuInS_2$ (cross-sectional view). All samples were prepared by repeating spin-coating/calcination steps nine times.

© 2024 The Author(s). Solar RRL published by Wiley-VCH GmbH

2367198x, 2024, 20, Downloaded from https://onlinelibrary.wiley.com/doi/10.1002/solr.202400518 by Cochrane Peru, Wiley Online Library on [01/10/2026]. See the Terms and Conditions (https://onlinelibrary.wiley.com/terms-and-conditions) on Wiley Online Library for rules of use; OA articles are governed by the applicable Creative Commons License

$CuInS_2$ was only found in the Ag-containing $CuInS_2$, but a peak shift to a lower angle was observed depending on the Ag content, which can be attributed to the lattice distortion of the Ag-doped $CuInS_2$ crystal (Figure 4b).[46] This observation indicates that Ag was successfully doped into the $CuInS_2$ lattice without the formation of another phase.

Figure 4c–f shows a grain size comparison of undoped and Ag-doped $CuInS_2$ using SEM images. Interestingly, the surface of the 3% Ag-doped $CuInS_2$ became less porous, with a reduced crack structure. Moreover, the cross-sectional SEM image clearly confirmed that Ag doping boosted crystal growth, resulting in a larger grain size of $CuInS_2$. Notably, the grains at the subsurface of the Ag-doped $CuInS_2$ also became significantly larger than those of undoped $CuInS_2$. This behavior was observed in Ag-doped $CuInS_2$, regardless of the Ag content (Figure S11, Supporting Information). In addition, no noticeable difference was observed in the morphology or particle size of Cu–In–O after Ag doping (Figure S12, Supporting Information). Therefore, Ag doping affected the sulfurization steps by activating recrystallization; however, it did not affect the grain growth of Cu–In–O during the preannealing steps under a N_2 atmosphere. In addition, the effect of Ag doping on optical properties was also confirmed using Kubelka–Munk absorbance. There was no noticeable difference in absorbance, but a slightly increased bandgap was observed with increasing Ag doping concentration (1.45–1.5 eV) (Figure S13, Supporting Information).

The PEC activity of the Ag-doped $CuInS_2$ was measured through LSV, and the photocurrent density was compared with the doping concentration of Ag (**Figure 5**a,b). The 3% Ag-doped $CuInS_2$ exhibited the highest photocurrent of -7.69 mA cm^{-2} at 0 V_{RHE}. This could be attributed to efficient charge carrier transport, which minimizes recombination at the grain boundaries. The grain size was similar for all Ag-doped $CuInS_2$; however, significantly high concentrations (5% and 10%) of Ag dopants had a negative effect on the photocurrent. The Mott–Schottky analysis was also performed on undoped and Ag-doped $CuInS_2$ (Figure S14, Supporting Information). Low concentrations of Ag doping (1% and 3%) merely affect the slope and intercept of the Mott–Schottky results compared to that of undoped $CuInS_2$, but the intercept was positively shifted for 5% and 10% Ag-doped $CuInS_2$. This implies that the improved PEC activity after Ag doping is mainly due to the enhanced grain growth, not the increase in carrier concentrations or changes in the band structure of the $CuInS_2$ up to ≈3% doping. However, excess Ag concentrations lead to changes in the band position or flat band potential due to crystal distortion, which may relate to the poor photoactivity of the 5% and 10% Ag-doped $CuInS_2$. To understand the charge transfer, electrochemical impedance spectroscopy was performed on the undoped and Ag-doped $CuInS_2$ photoelectrodes to estimate the charge transfer resistance (Figure 5c). The trend of the resistance values, estimated from the end of the right intercept of a semicircle, was similar to that of the photocurrent values of the undoped and Ag-doped $CuInS_2$ (i.e., 318.7, 297.3, 264.6, 361.5, and 396.4 Ω for undoped, 1%, 3%, 5%, and 10%, respectively). These results imply that Ag doping has another side effect such as the addition of recombination center in $CuInS_2$ lattice. Generally, heteroatoms in the lattice can enhance conductivity but also act as recombination centers. Therefore, only a suitable dopant concentration can enhance the PEC activity.

In addition, n-type CdS and TiO_2 protective layers were deposited on 3% Ag-doped $CuInS_2$ to enhance its PEC activity and

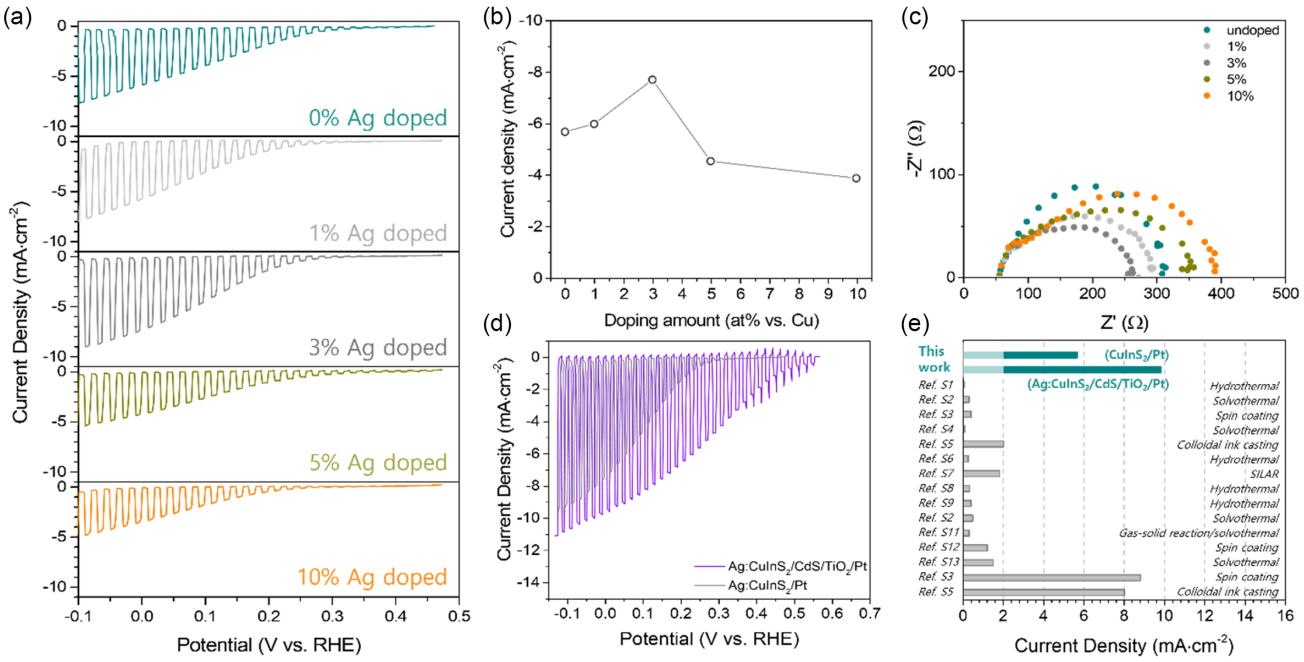

Figure 5. a) LSV results of undoped and Ag-doped $CuInS_2$ photoelectrodes. b) Comparison of the photocurrent of $CuInS_2$ depending on the concentration of Ag atoms. c) Nyquist plot of electrochemical impedance spectroscopy from undoped and Ag-doped $CuInS_2$ photoelectrodes. d) LSV results of $CuInS_2$/Pt and 3% Ag-doped $CuInS_2$/CdS/TiO_2/Pt photoelectrodes. e) Photocurrent comparison of the $CuInS_2$ synthesized by wet chemical-based methods (spin coating, hydrothermal, etc.).

© 2024 The Author(s). Solar RRL published by Wiley-VCH GmbH

2367198x, 2024, 20, Downloaded from https://onlinelibrary.wiley.com/doi/10.1002/solr.202400518 by Cochrane Peru, Wiley Online Library on [01/10/2026]. See the Terms and Conditions (https://onlinelibrary.wiley.com/terms-and-conditions) on Wiley Online Library for rules of use; OA articles are governed by the applicable Creative Commons License

stability. When a CdS layer is deposited on p-$CuInS_2$, an additional p–n junction generates a photovoltage and increases the onset potential and photocurrent.[47] TiO_2 is a well-known layer that protects against photocorrosion during a PEC reaction.[48] Cross-sectional SEM images and XPS depth profile are confirming that TiO_2/CdS was uniformly deposited on Ag-doped $CuInS_2$ (Figure S15, Supporting Information). After the CdS and TiO_2 deposition, the photocurrent increased to $-9.8\,mA\,cm^{-2}$ at 0 V_{RHE}, and the onset potential was positively shifted by ≈300 mV (Figure 5d). In addition, the PEC stability of the Ag-doped $CuInS_2$/CdS/TiO_2/Pt photocathode is increased from that of the Ag:$CuInS_2$/pt due to the presence of a protective TiO_2 layer (Figure S16, Supporting Information). Importantly, comparing the photocurrent at a potential of 0 V versus RHE with previously reported $CuInS_2$-based photoelectrodes, it was found that Ag-doped $CuInS_2$/CdS/TiO_2/Pt exhibits superior performance. This electrode stands out as the most efficient among $CuInS_2$-based photoelectrodes synthesized via wet chemical methods, including spin coating, hydrothermal, solvothermal, drop casting, and others, in terms of the photocurrent for the HER (Figure 5e and Table S1, Supporting Information). In addition, half-cell applied bias photon-to-current efficiency (HC-ABPE) is an important indicator for comparing the activity of photocathodes for solar-to-hydrogen conversion. The maximum HC-ABPE of the Ag:$CuInS_2$ was 0.47% at 0.12 V_{RHE}, but it is increased by more than 3 times after CdS and TiO_2 deposition on the Ag:$CuInS_2$ (1.41% at 0.26 V_{RHE}) (Figure S17, Supporting Information). The increased and positively shifted maximum HC-ABPE implies that the Ag-doped $CuInS_2$/CdS/TiO_2/Pt photocathode has higher potential for efficient solar-to-hydrogen conversion compared to the Ag:$CuInS_2$ photocathode when external bias is supplied to the PEC cell.

Finally, bias-free water splitting for H_2 production was performed using a $CuInS_2$ photoelectrode. We successfully

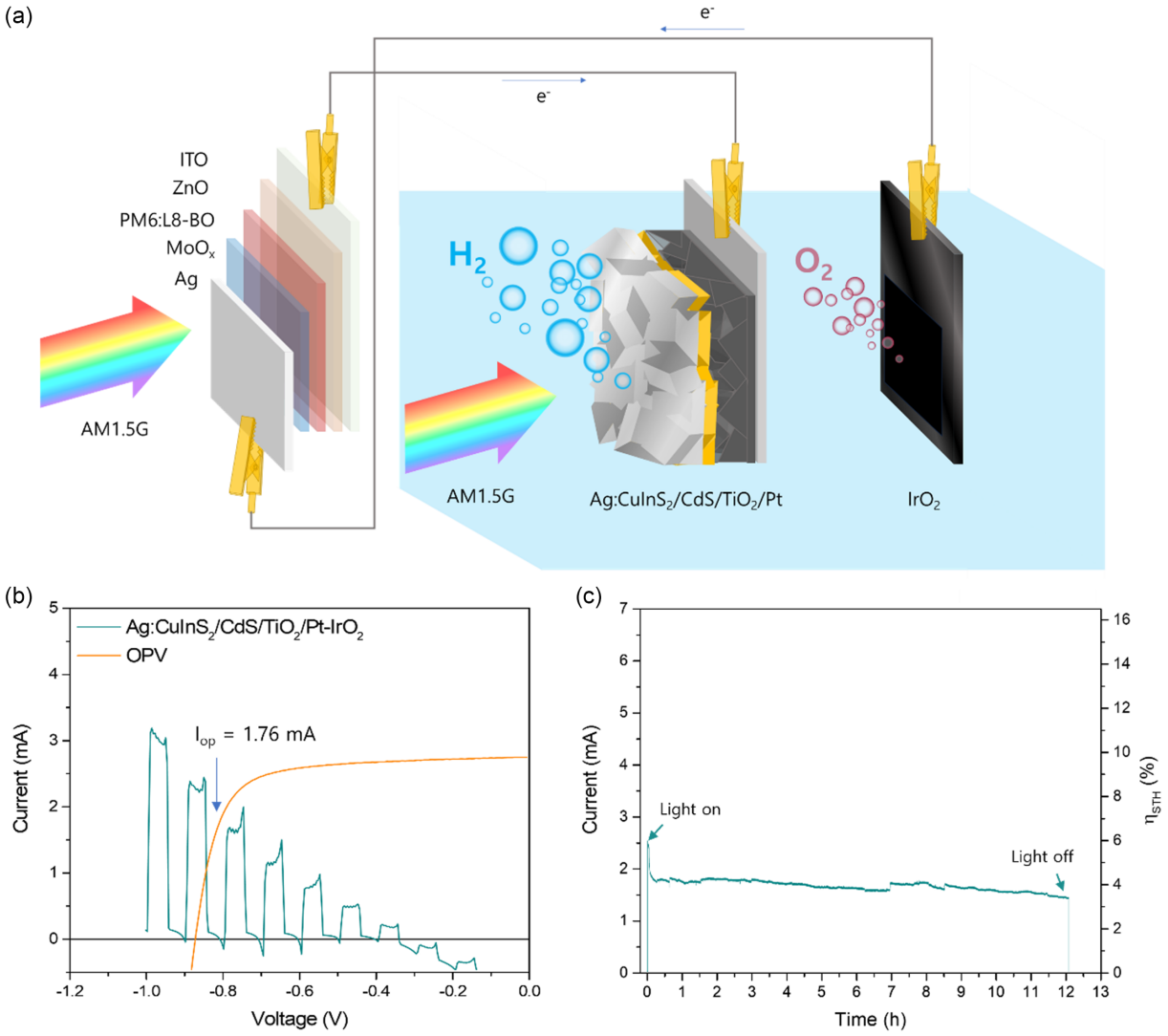

Figure 6. a) Schematic diagram of a PV–PEC cell for water splitting. b) *I–V* curve of OPV and an Ag:$CuInS_2$/CdS/TiO_2/Pt|IrO_2 cell. c) Chronoamperometry result at 0 V and solar-to-hydrogen conversion efficiency of the PV–PEC cell. The solar-to-hydrogen conversion efficiency is calculated from current values during cell configuration.

© 2024 The Author(s). Solar RRL published by Wiley-VCH GmbH

2367198x, 2024, 20, Downloaded from https://onlinelibrary.wiley.com/doi/10.1002/solr.202400518 by Cochrane Peru, Wiley Online Library on [01/10/2026]. See the Terms and Conditions (https://onlinelibrary.wiley.com/terms-and-conditions) on Wiley Online Library for rules of use; OA articles are governed by the applicable Creative Commons License

Table 1. Comparisons for PV–PEC cells.

PV–PEC cell (chemical-based approaches)					
Photoelectrode	Anode or cathode	Solar cell	Method[a)]	η_{STH}[c)]	References
Ag:$CuInS_2$/CdS/TiO_2/Pt (photocathode)	IrO_2	OPV (PM6:L8-BO)	Spin-coating	4.15	This work
$BiVO_4$(photoanode)	H_2ase	Perovskite	Electrodeposition	1.1	[49]
Si:Fe_2O_3/Al_2O_3/CoO_x (photoanode)	Pt	DSSC	APCVD	1.17	[9]
Mn:Fe_2O_3/Co–Pi	Pt	Perovskite ($CH_3NH_3PbI_3$)	Hydrothermal	2.4	[10]
Cu_2O/Al:ZnO/TiO_2/RuO_2 (photocathode)	IrO_2	Perovskite	Electrodeposition	2.5	[50]
$BiVO_4$/Co–Pi (Photoanode)	Pt	Perovskite ($CH_3NH_3PbI_3$)	Metal–organic decomposition	2.5	[51]
Fe_2O_3/SnO_x/FeOOH (photoanode)	Pt	Perovskite ($CH_3NH_3PbI_3$)	Hydrothermal	3.4	[11]
H_2-treated $BiVO_4$/Co–Ci	Pt	Perovskite ($CH_3NH_3PbI_3$)	Metal–organic decomposition	4.3	[52]
CuSCN/Cu_2O/Ga_2O_3/TiO_2/RuO_x (photocathode)	IrO_x	Perovskite	Electrodeposition	4.55	[53]
W:$BiVO_4$ (photoanode)	Pt	c-Si	Spray pyrolysis	4.9	[54]
$BiVO_4$/NiOOH/FeOOH	Pt	Perovskite ($Cs_{0.05}(FA_{0.83}MA_{0.17})_{0.95}Pb(I_{0.83}Br_{0.17})_3$)	Electrodeposition	6.5	[14]
WO_3/W,Mo:$BiVO_4$/NiOOH/FeOOH (photoanode)	Pt	DSSC	Spin-coating	7.1	[55]
$BiVO_4$/FeOOH/NiOOH‖Fe_2O_3/$NiFeO_x$ (photoanode)	Pt	c-Si	Metal–organic decomposition/ polymer-assisted nitrate decomposition method	7.7	[56]
$BaSnO_3$/NiOOH/FeOOH	Pt	Perovskite	Sol–gel	7.9	[57]
PV–PEC cell (physical-based approaches)					
Photoelectrode	Anode or cathode	Solar cell	Method[a)]	η_{STH}[c)]	References
Cu(In,Ga)Se_2/CdS/ZnO/TiO_2/Pt (photocathode)	DSA	Perovskite ($CH_3NH_3PbI_3$)	Coevaporation	2.6	[58]
Cu(In,Ga)Se_2/CdS/ZnO/TiO_2/Pt (photocathode)	DSA	Perovskite ($CH_3NH_3PbBr_3$)	Coevaporation	6.3	[58]
Ta_3N_5/$NiFeO_x$ (photoanode)	Pt	$CuInSe_2$	Sputtering	7	[15]
Cu(In,Ga)$(S,Se)_2$/ZnS/CdS/Pt (photocathode)	IrO_x	Perovskite	Cosputtering	8.17	[59]
(Ga,In)P/(Al,In)P/(Ga,In)P/Pt (photocathode)	RuO_x	(Ga,In)As	AP-MOVPE	16.2	[60]
PEC–PEC cell					
Photocathode	Photoanode	Method[b)]		η_{STH}[c)]	References
$CuGaO_2$/RBG-174/CoHEC	TaON/CoO_x	Drop-casting/electrophoresis		0.0054	[61]
$(CuGa)_{0.8}Zn_{0.4}S_2$/Ru	$BiVO_4$/CoO_x	Solid-state reaction/solid-state reaction		0.016	[62]
ZnSe:CIGS/RuO_x	Mg:Ta_3N_5/$NiFeO_x$	Coevaporation/spin-coating		≈0.06	[63]
Cu_2O/Al:ZnO/TiO_2/RuO_x	W:$BiVO_4$/Co–Pi	Electrodeposition/spray pyrolysis		0.5	[64]
(Ag,Cu)$GaSe_2$/$CuGa_3Se_5$/CdS/Pt	Mo:$BiVO_4$/FeOOH/NiOOH	Coevaporation/metal–organic decomposition		0.67	[65]
a-Si	Fe_2O_3/$NiFeO_x$	-/Hydrothermal		0.91	[66]
$CuInGaSe_2$/CdS/Al_2O_3/TiO_2/Pt	$BiVO_4$/FeOOH/NiOOH	Coevaporation/electrodeposition		1.01	[4]
Cu_2O/Ga_2O_3/TiO_2/RuO_x	Mo:$BiVO_4$/$NiFeO_x$	Electrodeposition/metal–organic decomposition		3	[5]
Cu_2ZnSnS_4/HfO_2/CdS/HfO_2/Pt	$BiVO_4$	Spray pyrolysis/spray pyrolysis		3.17	[6]

[a)]Preparation method for photoabsorber semiconductor material; [b)]Preparation method for photocathode/photoanode semiconductor material; [c)]Solar to hydrogen conversion efficiency without applied bias.

prepared highly active $CuInS_2$ by controlling the synthesis parameters. However, $CuInS_2$ cannot intrinsically split water without an external bias owing to the energy-level mismatch of the band structure to the standard reduction potential of water oxidation (1.23 V_{RHE}). Therefore, a PV–PEC cell was configured for bias-free water splitting. First, a PEC cell with a $CuInS_2$-based photocathode and anode was prepared. Subsequently, an organic PV cell was connected in parallel to the PEC cell. The PV cell supplies an electrical bias to the PEC cell, as shown in **Figure 6**a and S18, Supporting Information. Before the operation

© 2024 The Author(s). Solar RRL published by Wiley-VCH GmbH

2367198x, 2024, 20, Downloaded from https://onlinelibrary.wiley.com/doi/10.1002/solr.202400518 by Cochrane Peru, Wiley Online Library on [01/10/2026]. See the Terms and Conditions (https://onlinelibrary.wiley.com/terms-and-conditions) on Wiley Online Library for rules of use; OA articles are governed by the applicable Creative Commons License

of the PV–PEC cell, the performances of the PEC and PV cells were investigated (Figure 6b). For the PEC cell, a 3% Ag-doped $CuInS_2/CdS/TiO_2/Pt$ photocathode was coupled to a commercial IrO_2 anode. The LSV curve of the Ag:$CuInS_2/CdS/TiO_2/Pt$ | IrO_2 cell was measured using a two-electrode configuration. In the case of the PV cell, the power conversion efficiency was 12.61%, J_{sc} was 19.93 mA cm^{-2}, V_{oc} was 0.868, and the fill factor was 72.94%. The intersection of the *I–V* curves of the PV and PEC cells indicated the operational current when the PV and PEC cells were connected in series. The operational current (I_{op}) was 1.76 mA.

Figure 6c shows the operation of the PV–PEC cell without external bias. The photocurrent was generated by simulated solar light illumination, and the current was similar to that of I_{op} in Figure 6b. During the reaction, Faradaic efficiency for H_2 and O_2 was obtained for initial 400 min (Figure S19, Supporting Information). The η_{STH} of the PV–PEC cell was estimated by the following equation:

$$\eta_{STH}(\%) = \frac{I(\text{mA}) \times 1.23(V) \times \eta_{H_2}}{(A_{PEC}(\text{cm}^2) + A_{PV}(\text{cm}^2))} \div 1\ \text{sun}\ (\text{mW} \times \text{cm}^{-2}) \times 100\% \quad (1)$$

where I is the photocurrent at 0 V, η_{H_2} is the Faradaic efficiency (99.5%/100% = 0.995), A_{PEC} is the active area of the photoelectrode (0.3848 cm^2), A_{PV} is the active area of the PV cell (0.12 cm^2), and 1 sun is the illumination power density. The initial η_{STH} was 4.15%, and it decreased to 3.35% after 12 h. This is the first demonstration of a PV–PEC cell for bias-free water splitting using a $CuInS_2$ photocathode. Moreover, this result shows comparable η_{STH} to those of PV–PEC or PEC tandem cells employing chalcopyrite or wet chemical method-based photoelectrodes (**Table 1**). This result shows that $CuInS_2$ has great potential for PEC H_2 production if its PEC activity can be further improved through additional investigations.

3. Conclusion

In this study, $CuInS_2$ photoelectrodes were prepared using a cost-effective and scalable wet chemical spin-coating method. The grain size of $CuInS_2$ was meticulously engineered by controlling parameters such as atomic ratio, thickness, morphology, and Ag doping. This resulted in enlarged crystal grains and improved charge transfer. The novel growth mechanism of $CuInS_2$ from Cu-In-O was also investigated, which confirmed that Ag doping significantly enhanced grain growth. Consequently, the $CuInS_2$ photocathode exhibited one of the highest PEC activities among those prepared using wet chemical approaches. Furthermore, we successfully demonstrated bias-free water splitting using a $CuInS_2$-based photoelectrode in a PV–PEC cell configuration. These results highlight the substantial potential of $CuInS_2$, prepared through wet chemical methods, for cost-effective PEC water splitting.

4. Experimental Section

Preparation of $CuInS_2$ Thin Films: $CuInS_2$ films were prepared by spin coating and subsequent sulfurization on Mo-deposited (500 nm thickness) soda–lime glass (**Scheme 1**). The precursor ink was coated onto the precleaned substrates using a spin coater at 2000 rpm for 60 s. The spin-coated substrate was calcined at 300 °C for 30 min with a ramping rate of 10 °C min^{-1} in an air atmosphere. After the spin-coating–calcination step, the calcined film was annealed at 110 °C for 1 h in the N_2 atmosphere, and then subsequently sulfurized at 520 °C for 40 min in the 1% H_2S/N_2 atmosphere for $CuInS_2$ formation (refer to details in **Scheme 2**). The spin-coating/calcination process was repeated before the sulfurization step to control the thickness of the $CuInS_2$ films. The sulfurized film was etched in 0.1 M KCN for 30 s and rinsed with distilled water. For the preparation of the precursor ink, $Cu(NO_3)_2{\cdot}xH_2O$, 1.6 g $In(NO_3)_3{\cdot}xH_2O$, and 1 g poly(vinyl acetate) (average $M_w \approx 100\,000$, Sigma–Aldrich) were dissolved in 14 mL methanol. The amount of $Cu(NO_3)_2{\cdot}xH_2O$ was adjusted by 0.7125–1.23 g for controlling the atomic ratio of Cu/In. For Ag doping, $Ag(NO_3)$ was dissolved in the precursor ink at 1–10 at% versus the amount of Cu in the ink.

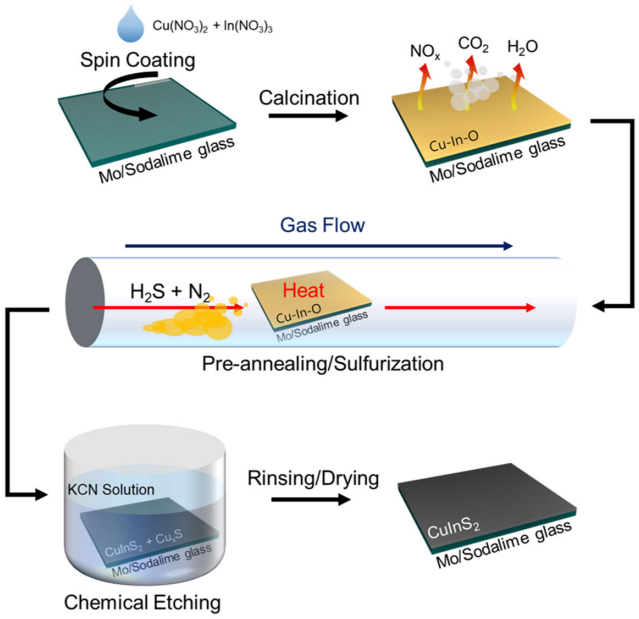

Scheme 1. Schematic diagram of the preparation procedure of $CuInS_2$ thin film.

CdS and TiO_2 Deposition on Ag-Doped $CuInS_2$ Thin Films: The CdS layer was deposited via chemical bath deposition. An Ag-doped $CuInS_2$ film was kept in a chemical bath containing a mixture of a 0.05 M $CdSO_4$ aqueous solution (20 mL) and a 30% NH_4OH aqueous solution (26 mL). The bath temperature was increased to 60 °C; then, 0.1 M thiourea aqueous solution (10 mL) was added to the bath. The Ag-doped $CuInS_2$ film was then removed from the chemical bath after 10 min. TiO_2 (50 nm) was deposited on the CdS-deposited Ag-doped $CuInS_2$ using an e-beam evaporator (KVE-E2006, Korea Vacuum Tech.) with TiO_2 pellets.

Characterization: The PEC hydrogen evolution reaction was performed using a potentiostat (Iviumstat, Ivium Technology) with a three-electrode configuration ($CuInS_2$ films as a working electrode, Ag/AgCl as a reference electrode, and Pt as a counter electrode) in a 0.1 M $HClO_4$ electrolyte (pH 1.08). LSV was performed under chopped simulated sunlight (AM1.5G, 100 mW cm^{-2}). Simulated sunlight was generated using a solar simulator (AbetSun 2000, Abet Technology). Before the LSV measurement of the $CuInS_2$ films, Pt cocatalysts were electrodeposited on the $CuInS_2$ film using a potentiostat with a three-electrode system in a 1 mM $H_2PtCl_6{\cdot}6H_2O$ aqueous solution (−0.1 V, 45 s). Electrochemical impedance spectroscopy was performed at 0 V_{RHE}, within the frequency range of 10^6 to 0.01 Hz under 1 sun illumination. The electrical potential scale was converted into a reversible hydrogen electrode using Equation (2):

© 2024 The Author(s). Solar RRL published by Wiley-VCH GmbH

2367198x, 2024, 20, Downloaded from https://onlinelibrary.wiley.com/doi/10.1002/solr.202400518 by Cochrane Peru, Wiley Online Library on [01/10/2026]. See the Terms and Conditions (https://onlinelibrary.wiley.com/terms-and-conditions) on Wiley Online Library for rules of use; OA articles are governed by the applicable Creative Commons License

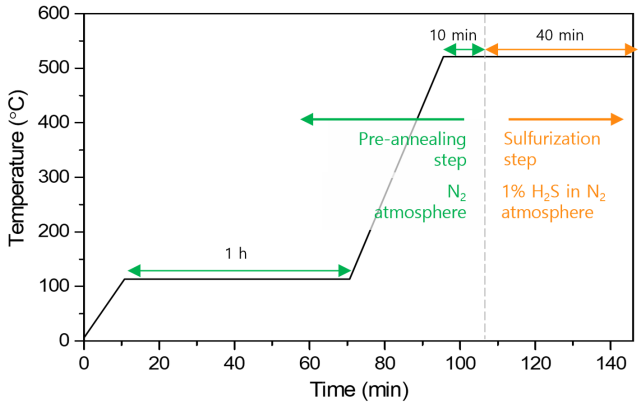

Scheme 2. Temperature profile for a sulfurization process.

$$E_{RHE}(V) = E_{app}(V) + (0.0591\,pH) + E^{\circ}_{Ag/AgCl}(V) \quad (2)$$

where E_{app} is the applied potential versus the Ag/AgCl reference electrode, pH indicates the pH of the electrolyte, and $E^{\circ}_{Ag/AgCl}$ is the standard potential of the Ag/AgCl reference electrode (0.209 V_{NHE}). Mott–Schottky analysis was performed on the photocathode using a potentiostat with an AC potential frequency of 1000 Hz in a 0.1 M $HClO_4$ electrolyte with a three-electrode configuration under dark conditions.

HC-ABPE was calculated using Equation (3):

$$\text{HC-ABPE}\,(\%) = \frac{\left[E_{app}(V) - E^{\circ}_{H^+/H_2}(V)\right] \times J(mA \times cm^{-2})}{P(mW \times cm^{-2})} \times 100\% \quad (3)$$

where E_{app} is the applied potential, $E^{\circ}_{H^+/H_2}$ is the standard reduction potential of HER, J is the photocurrent density of the photocathode, and P is the power density of incident light.

For Faradaic efficiency measurement, the evolved H_2 and O_2 in the reactor were injected into a gas chromatograph (YL6500, Younglin). The Faradaic efficiency of H_2 and O_2 was calculated using Equation (4):

$$\text{Faradaic efficiency}\,(\%) = \frac{n \times F \times P \times R^{-1} \times T^{-1} \times Q \times \varphi}{I_{ph}} \times 100\% \quad (4)$$

where n is the number of equivalent electrons for H^+/H_2 or H_2O/O_2 (2 or 4), F is the Faraday constant, P is the reactor pressure, R is the gas constant, T is the reactor temperature, Q is the flow rate of the injected gas (20 min^{-1}), φ is the concentration of the product gas, and I_{ph} is the photocurrent of the PV–PEC cell.

Field-emission SEM was performed using an Inspect F50 microscope for material characterization. Grazing incidence XRD patterns were obtained with Dmax2500/PC. The chemical states of the samples were determined using an XPS with a Nexsa, ThermoFisher Scientific). The Kubelka–Munk absorbance of the $CuInS_2$ thin film was obtained from diffuse reflectance measurements using a UV–vis spectrophotometer (Model 2600/2700, Shimadzu) equipped with an integrating sphere. XPS was performed using a Nexsa (ThermoFisher Scientific) with sputtering by a 2 kV Ar^+ ion beam.

Preparation of Organic Photovoltaic Cells and IrO_2 Anodes for PV–PEC Cells: The organic photovoltaics (OPVs) were fabricated using an indium tin oxide (ITO)/ZnO sol–gel/PM6:L8-BO/MoO_x/Ag structure. The ITO substrate was cleaned by sonication in isopropanol, deionized water, acetone, and isopropanol for 10 min each and then dried in an oven for 2 h. The precleaned ITO substrate was cleaned by UV–ozone treatment for 30 min. The ITO substrate was then spin-coated with a ZnO sol–gel solution at 5000 rpm for 40 s and annealed at 200 °C in air for 30 min. After annealing, the substrates were transferred to a glove box. Separately, the PM6:L8-BO blend (1.0:1.2 w/w) was dissolved in chloroform containing 0.4 vol% 1-fluoronaphthalene at a concentration of 11.0 mg mL^{-1}. The blend solution was stirred at 60 °C for 1 h and at 40 °C for another 1 h. The blend solution was then spin-coated on the ITO/ZnO substrate at 5000 rpm for 30 s. For the ITO/ZnO/PM6:L8-BO blend films, thermal annealing was performed at 90°Cfor 10 min. Finally, MoO_3 (6 nm) and Ag (150 nm) were sequentially deposited through a shadow mask of 13.7 mm^2 at 5×10^{-6} Torr. The active area of the OPV was 0.12 cm^2

The IrO_2 anode was prepared through drop casting. To this end, 96.8 mg IrO_2(Alfa Aesar, Premion, 99.99%) was dispersed in a mixture of 1.8 mL H_2O, 0.64 mL isopropanol, and 60 µL Nafion117 containing solution (Sigma–Aldrich, ≈5% in a mixture of lower aliphatic alcohols and water) for ink preparation. Then, 68 µL of the ink was dropped on a glassy carbon substrate (active area 2.25 cm^2) and dried at 60 °C for 1 h.

Supporting Information

Supporting Information is available from the Wiley Online Library or from the author.

Acknowledgements

This study was supported by the Korea Institute of Science and Technology (grant no. 2E33251). This work was supported by the program of Future Hydrogen Original Technology Development (grant no. NRF-2021M3I3A1082879) through the National Research Foundation of Korea (NRF) funded by the Korean government (Ministry of Science and ICT). This research was supported by the Basic Science Research Program through the National Research Foundation of Korea (NRF) funded by the Ministry of Education (grant no. RS-2023-00249042). This research was supported by the Basic Science Research Program through the National Research Foundation of Korea (NRF) funded by the Ministry of Education (grant no. 2023R1A2C3006550). This research was supported by Global Learning & Academic Research Institution for Master's,·Ph.D. students, and Postdocs (G-LAMP) Program of the National Research Foundation of Korea (NRF) grant funded by the Ministry of Education (grant no. RS-2023-00285390).

Conflict of Interest

The authors declare no conflict of interest.

Author Contributions

Sang Youn Chae: Conceptualization (lead); Investigation (lead); Methodology (lead); Project administration (supporting); Writing—original draft (lead); Writing—review and editing (equal). **Noyoung Yoon**: Data curation (lead); Investigation (lead); Visualization (equal); Writing—original draft (equal). **Minki Jun**: Data curation (supporting); Methodology (supporting); Project administration (supporting); Visualization (lead); Writing—original draft (supporting); Writing—review and editing (supporting). **Sung Hyun Hur**: Data curation (supporting); Investigation (supporting). **Myeongjae Lee**: Data curation (supporting); Formal analysis (supporting); Investigation (supporting). **BongSoo Kim**: Formal analysis (supporting); Writing—review and editing (equal). **Jin Young Kim**: Project administration (equal); Visualization (equal); Writing—review and editing (equal). **Eun Duck Park**: Project administration (equal); Supervision (equal); Validation (lead); Writing—review and editing (equal). **Jong Hyeok Park**: Supervision (equal); Validation (equal); Visualization (equal); Writing—review and editing (lead). **Oh-Shim Joo**: Project administration (equal); Supervision (lead); Validation (equal); Writing—review and editing (equal). **Sang Youn Chae** and **Noyoung Yoon**: contributed equally to this work.

© 2024 The Author(s). Solar RRL published by Wiley-VCH GmbH

2367198x, 2024, 20, Downloaded from https://onlinelibrary.wiley.com/doi/10.1002/solr.202400518 by Cochrane Peru, Wiley Online Library on [01/10/2026]. See the Terms and Conditions (https://onlinelibrary.wiley.com/terms-and-conditions) on Wiley Online Library for rules of use; OA articles are governed by the applicable Creative Commons License

Data Availability Statement

The data that support the findings of this study are available from the corresponding author upon reasonable request.

Keywords

$CuInS_2$, green hydrogen, photoelectrochemical cells, photovoltaic–photoelectrochemical cells, spin coating

Received: July 13, 2024
Revised: August 8, 2024
Published online: August 26, 2024

[1] M. S. Dresselhaus, I. L. Thomas, *Nature* **2001**, *414*, 332.
[2] C. Jiang, S. J. A. Moniz, A. Wang, T. Zhang, J. Tang, *Chem. Soc. Rev.* **2017**, *46*, 4645.
[3] K. T. Fountaine, H. J. Lewerenz, H. A. Atwater, *Nat. Commun.* **2016**, *7*, 13706.
[4] M. Chen, Y. Liu, C. Li, A. Li, X. Chang, W. Liu, Y. Sun, T. Wang, J. Gong, *Energy Environ. Sci.* **2018**, *11*, 2025.
[5] L. Pan, J. H. Kim, M. T. Mayer, M.-K. Son, A. Ummadisingu, J. S. Lee, A. Hagfeldt, J. Luo, M. Grätzel, *Nat. Catal.* **2018**, *1*, 412.
[6] D. Huang, K. Wang, L. Li, K. Feng, N. An, S. Ikeda, Y. Kuang, Y. Ng, F. Jiang, *Energy Environ. Sci.* **2021**, *14*, 1480.
[7] M. S. Prévot, K. Sivula, *J. Phys. Chem. C* **2013**, *117*, 17879.
[8] M. G. Walter, E. L. Warren, J. R. McKone, S. W. Boettcher, Q. Mi, E. A. Santori, N. S. Lewis, *Chem. Rev.* **2010**, *110*, 6446.
[9] J. Brillet, J.-H. Yum, M. Cornuz, T. Hisatomi, R. Solarska, J. Augustynski, M. Graetzel, K. Sivula, *Nat. Photonics* **2012**, *6*, 824.
[10] D. Sabba, M. H. Kumar, L. H. Wong, J. Barber, M. Grätzel, N. Mathews, *Nano Lett.* **2015**, *15*, 3833.
[11] R. A. John, P. P. Boix, C. Yi, C. Shi, M. C. Scott, S. A. Veldhuis, A. M. Minor, S. M. Zakeeruddin, L. H. Wong, M. Grätzel, N. Mathews, *ChemSusChem* **2017**, *10*, 2449.
[12] J. Park, K.-Y. Yoon, T. Kim, H. Jang, M.-J. Kwak, J. Y. Kim, J.-H. Jang, *Nano Energy* **2020**, *76*, 105089.
[13] L. Han, F. F. Abdi, R. van de Krol, R. Liu, Z. Huang, H.-J. Lewerenz, B. Dam, M. Zeman, A. H. M. Smets, *ChemSusChem* **2014**, *7*, 2832.
[14] S. Wang, P. Chen, Y. Bai, J.-H. Yun, G. Liu, L. Wang, *Adv. Mater.* **2018**, *30*, 1800486.
[15] T. Higashi, H. Nishiyama, Y. Suzuki, Y. Sasaki, T. Hisatomi, M. Katayama, T. Minegishi, K. Seki, T. Yamada, K. Domen, *Angew. Chem., Int. Ed.* **2019**, *58*, 2300.
[16] Y. Kawase, T. Higashi, K. Domen, K. Takanabe, *Adv. Energy Sustainability Res.* **2021**, *2*, 2100023.
[17] J. E. Jaffe, A. Zunger, *Phys. Rev. B* **1984**, *29*, 1882.
[18] N. Yoon, O. S. Joo, S. Y. Chae, E. D. Park, *Nanomaterials* **2023**, *13*, 1361.
[19] Q. Cai, Z. Liu, C. Ma, Z. Tong, C. Han, *J. Mater. Sci.: Mater. Electron.* **2018**, *29*, 20629.
[20] M. Li, R. Zhao, Y. Su, J. Hu, Z. Yang, Y. Zhang, *Adv. Mater. Interfaces* **2016**, *3*, 1600494.
[21] W. Septina, N. M. Nursam, J. P. Lopes, N. Gaillard, *J. Electroanal. Chem.* **2023**, *940*, 117484.
[22] M. Li, L. Chen, Y. Su, H. Yin, K. Hu, *J. Energy Chem.* **2020**, *51*, 134.
[23] N. Guijarro, M. S. Prévot, X. Yu, X. A. Jeanbourquin, P. Bornoz, W. Bourée, M. Johnson, F. Le Formal, K. Sivula, *Adv. Energy Mater.* **2016**, *6*, 1501949.
[24] Q. Cai, Z. Liu, C. Han, Z. Tong, C. Ma, *J. Alloys Compd.* **2019**, *795*, 319.
[25] Z. Liu, X. Lu, D. Chen, *ACS Sustainable Chem. Eng.* **2018**, *6*, 10289.
[26] Z. Liu, M. Zhou, *ACS Sustainable Chem. Eng.* **2020**, *8*, 512.
[27] S. Kumar, N. Yadav, P. Kumar, A. K. Ganguli, *Inorg. Chem.* **2018**, *57*, 15112.
[28] M. Li, R. Zhao, Y. Su, J. Hu, Z. Yang, Y. Zhang, *Appl. Catal., B* **2017**, *203*, 715.
[29] M. Kumar, B. Meena, P. Subramanyam, G. Ummethala, S. R. K. Malladi, S. Dutta-Gupta, C. Subrahmanyam, *Energy Fuels* **2023**, *37*, 2340.
[30] F. Amano, T. Ebina, B. Ohtani, *Electrochemistry* **2011**, *79*, 804.
[31] Y. Zhao, S. Yuan, Q. Chang, Z. Zhou, D. Kou, W. Zhou, Y. Qi, S. Wu, *Adv. Funct. Mater.* **2021**, *31*, 2007928.
[32] N. Gaillard, W. Septina, J. Varley, T. Ogitsu, K. K. Ohtaki, H. A. Ishii, J. P. Bradley, C. Muzzillo, K. Zhu, F. Babbe, J. Cooper, *Mater. Adv.* **2021**, *2*, 5752.
[33] A. Urbaniak, A. Czudek, A. Eslam, R. Wuerz, M. Igalson, *Sol. Energy Mater. Sol. Cells* **2023**, *253*, 112252.
[34] O. Cojocaru-Mirédin, M. Raghuwanshi, R. Wuerz, S. Sadewasser, *Adv. Funct. Mater.* **2021**, *31*, 2103119.
[35] N. Ueoka, T. Oku, *ACS Appl. Mater. Interfaces* **2018**, *10*, 44443.
[36] S. Y. Chae, S. J. Park, S. G. Han, H. Jung, C.-W. Kim, C. Jeong, O.-S. Joo, B. K. Min, Y. J. Hwang, *J. Am. Chem. Soc.* **2016**, *138*, 15673.
[37] R. Adi Wijaya, A. Suseno, R. A. Lusiana, W. Septina, T. Harada, *J. Electroanal. Chem.* **2023**, *945*, 117683.
[38] J. Zhao, T. Minegishi, L. Zhang, M. Zhong, M. Nakabayashi, G. Ma, T. Hisatomi, M. Katayama, S. Ikeda, N. Shibata, T. Yamada, K. Domen, *Angew. Chem., Int. Ed.* **2014**, *53*, 11808.
[39] T. Unold, I. Sieber, K. Ellmer, *Appl. Phys. Lett.* **2006**, *88*, 213502.
[40] H. Rodriguez-Alvarez, R. Mainz, B. Marsen, H.-W. Schock, *J. Solid State Chem.* **2010**, *183*, 803.
[41] D. Thomas, R. Mainz, H. Rodriguez-Alvarez, B. Marsen, D. Abou-Ras, M. Klaus, C. Genzel, H. W. Schock, *Thin Solid Films* **2011**, *519*, 7193.
[42] M. L. Fearheiley, N. Dietz, H. J. Lewerenz, *J. Electrochem. Soc.* **1992**, *139*, 512.
[43] T. Wada, N. Kohara, T. Negami, M. Nishitani, *J. Mater. Res.* **1997**, *12*, 1456.
[44] T. Walter, D. Braunger, H. Dittrich, C. Köble, R. Herberholz, H. W. Schock, *Sol. Energy Mater. Sol. Cells* **1996**, *41*, 355.
[45] L. E. Oikkonen, M. G. Ganchenkova, A. P. Seitsonen, R. M. Nieminen, *J. Appl. Phys.* **2013**, *113*, 133510.
[46] A. Werner, I. Luck, J. Bruns, J. Klaer, K. Siemer, D. Bräunig, *Thin Solid Films* **2000**, *361*, 88.
[47] S. Y. Chae, Y. Kim, E. D. Park, S. H. Im, O.-S. Joo, *ACS Appl. Mater. Interfaces* **2021**, *13*, 58447.
[48] A. Azarpira, M. Lublow, A. Steigert, P. Bogdanoff, D. Greiner, C. A. Kaufmann, M. Krüger, U. Gernert, R. van de Krol, A. Fischer, T. Schedel-Niedrig, *Adv. Energy Mater.* **2015**, *5*, 1402148.
[49] E. Edwardes Moore, V. Andrei, S. Zacarias, I. A. C. Pereira, E. Reisner, *ACS Energy Lett.* **2020**, *5*, 232.
[50] P. Dias, M. Schreier, S. D. Tilley, J. Luo, J. Azevedo, L. Andrade, D. Bi, A. Hagfeldt, A. Mendes, M. Grätzel, M. T. Mayer, *Adv. Energy Mater.* **2015**, *5*, 1501537.
[51] Y.-S. Chen, J. S. Manser, P. V. Kamat, *J. Am. Chem. Soc.* **2015**, *137*, 974.
[52] J. H. Kim, Y. Jo, J. H. Kim, J. W. Jang, H. J. Kang, Y. H. Lee, D. S. Kim, Y. Jun, J. S. Lee, *ACS Nano* **2015**, *9*, 11820.
[53] L. Pan, Y. Liu, L. Yao, R. Dan, K. Sivula, M. Grätzel, A. Hagfeldt, *Nat. Commun.* **2020**, *11*, 318.
[54] F. F. Abdi, L. Han, A. H. M. Smets, M. Zeman, B. Dam, R. van de Krol, *Nat. Commun.* **2013**, *4*, 2195.

© 2024 The Author(s). Solar RRL published by Wiley-VCH GmbH

2367198x, 2024, 20, Downloaded from https://onlinelibrary.wiley.com/doi/10.1002/solr.202400518 by Cochrane Peru, Wiley Online Library on [01/10/2026]. See the Terms and Conditions (https://onlinelibrary.wiley.com/terms-and-conditions) on Wiley Online Library for rules of use; OA articles are governed by the applicable Creative Commons License

[55] X. Shi, H. Jeong, S. J. Oh, M. Ma, K. Zhang, J. Kwon, I. T. Choi, I. Y. Choi, H. K. Kim, J. K. Kim, J. H. Park, *Nat. Commun.* **2016**, *7*, 11943.
[56] J. H. Kim, J.-W. Jang, Y. H. Jo, F. F. Abdi, Y. H. Lee, R. van de Krol, J. S. Lee, *Nat. Commun.* **2016**, *7*, 13380.
[57] M. Kim, B. Lee, H. Ju, J. Y. Kim, J. Kim, S. W. Lee, *Adv. Mater.* **2019**, *31*, 1903316.
[58] J. Luo, Z. Li, S. Nishiwaki, M. Schreier, M. T. Mayer, P. Cendula, Y. H. Lee, K. Fu, A. Cao, M. K. Nazeeruddin, Y. E. Romanyuk, S. Buecheler, S. D. Tilley, L. H. Wong, A. N. Tiwari, M. Grätzel, *Adv. Energy Mater.* **2015**, *5*, 1501520.
[59] B. Koo, D. Kim, P. Boonmongkolras, S. R. Pae, S. Byun, J. Kim, J. H. Lee, D. H. Kim, S. Kim, B. T. Ahn, S.-W. Nam, B. Shin, *ACS Appl. Energy Mater.* **2020**, *3*, 2296.
[60] J. L. Young, M. A. Steiner, H. Döscher, R. M. France, J. A. Turner, T. G. Deutsch, *Nat. Energy* **2017**, *2*, 17028.
[61] C. D. Windle, H. Kumagai, M. Higashi, R. Brisse, S. Bold, B. Jousselme, M. Chavarot-Kerlidou, K. Maeda, R. Abe, O. Ishitani, V. Artero, *J. Am. Chem. Soc.* **2019**, *141*, 9593.
[62] T. Kato, Y. Hakari, S. Ikeda, Q. Jia, A. Iwase, A. Kudo, *J. Phys. Chem. Lett.* **2015**, *6*, 1042.
[63] D. Akagi, Y. Kageshima, Y. Hashizume, S. Aoi, Y. Sasaki, H. Kaneko, T. Higashi, T. Hisatomi, M. Katayama, T. Minegishi, S. Noda, K. Domen, *ChemPhotoChem* **2019**, *3*, 521.
[64] P. Bornoz, F. F. Abdi, S. D. Tilley, B. Dam, R. van de Krol, M. Graetzel, K. Sivula, *J. Phys. Chem. C* **2014**, *118*, 16959.
[65] J. H. Kim, H. Kaneko, T. Minegishi, J. Kubota, K. Domen, J. S. Lee, *ChemSusChem* **2016**, *9*, 61.
[66] J.-W. Jang, C. Du, Y. Ye, Y. Lin, X. Yao, J. Thorne, E. Liu, G. McMahon, J. Zhu, A. Javey, J. Guo, D. Wang, *Nat. Commun.* **2015**, *6*, 7447.

© 2024 The Author(s). Solar RRL published by Wiley-VCH GmbH

2367198x, 2024, 20, Downloaded from https://onlinelibrary.wiley.com/doi/10.1002/solr.202400518 by Cochrane Peru, Wiley Online Library on [01/10/2026]. See the Terms and Conditions (https://onlinelibrary.wiley.com/terms-and-conditions) on Wiley Online Library for rules of use; OA articles are governed by the applicable Creative Commons License